Original Article

Influence of different soil properties on the failure behavior of deposit slope under earthquake after rainfall

YANG Bing* https://orcid.org/0000-0002-4098-1419; e-mail: yangb@home.swjtu.edu.cn

HOU Jiang-rong https://orcid.org/0000-0002-1984-9915 ; e-mail: jiangronghou@my.swjtu.edu.cn

ZHOU Zi-hong https://orcid.org/0000-0002-6985-793X; e-mail: 614951242@qq.com

GOU Jin-cheng https://orcid.org/0000-0003-1787-4241; e-mail:498229407@qq.com

Corresponding author

School of Civil Engineering, Southwest Jiaotong University, Chengdu 610031, China

Abstract: In this study, the influence of soil properties on the failure behavior and mechanism of slope under earthquake after rainfall was studied with shaking table test in the laboratory, in which the failure process of slope and instant responses of water content and pore water pressure were tested. Based on the principle of similarity, a model test was designed. The experimental results showed that soil properties exhibit significant influence on failure mode and failure mechanism of slope. Local flowslide, local failure, and creep flowslide failure modes appear in the slope exposed to only rainfall. However, under earthquake after rainfall, the other three failure modes occur, i.e., local slip failure, overall slip failure, and shallow scouring and creep flowslide failure. The spatial distribution of water content and pore water pressure are the two key factors leading to slope failure. Furthermore, due to the difference of permeability, the soil properties not only affect the spatial distribution of water content of the slope after rainfall, resulting in the peak pore water pressure which occurs mainly near the foot of the slope and near the bedrock interface in the middle and lower parts of the slope, but also affect the dissipation of excess pore water pressure in the process of earthquake. Finally, it is discovered that different types of soil lead to significant differences in the peak acceleration of slope failure. The critical acceleration of slope with coarse-grained soil is greater than that of slope with fine-grained soil. The critical acceleration of slope failure shows a close relationship with soil properties.

Keywords: Failure mode; Failure mechanism; Deposit slope; Soil properties; Earthquake after rainfall

1 Introduction

In earthquake-prone and rainfall-rich areas, post-rain earthquakes often occur. Rainfall leads to increase of the soil water content, and the following earthquake may induce large-scale landslides. A typical case of the earthquake-induced landslides after rainfall is the Niigata earthquake in Japan on October 23, 2004 (Sassa et al. 2007). Three days before the earthquake, a typhoon attacked the Niigata Prefecture, bringing a lot of rainfall (Sassa et al. 2007). Moreover, extreme rainfall events had

occurred frequently within one month before the earthquake. Eventually, the earthquake induced 362 landslides, among which 12 were large-scale landslides, and two landslides, namely, the Higashi–Takezawa landslide and the Terano landslide formed landslide dams of more than 25 m. At 17:16 on September 30, 2009, an earthquake (M_w 7.6) occurred in West Sumatra, Indonesia (Faris et al. 2014). Before the earthquake, the rainfall continued in the area (Faris et al. 2014). The earthquake triggered a large number of landslides and caused serious casualties, among which the largest landslides occurred in the Tandikat, Padang Pariaman Regency (Faris et al. 2014). Other examples have been reported by some researchers (Tian et al. 2016; Xu et al. 2016; Zhuang et al. 2020; Wang et al. 2021; Pu et al. 2021). Besides, the influence of earthquake on the stability of slopes has also been studied fully (Lin and Wang 2006; Qiu et al. 2017; Tiwari et al. 2017; Yang et al. 2019; Yang et al. 2021).

Before the 5·12 earthquake in 2008, Sichuan had been in the annual flood season in May. The meteorological data (Song et al. 2009; Shi et al. 2010) showed that ample rainfall had occurred in the Longmen Mountain fault belt before the 5·12 earthquake. Therefore, the soil water content before the earthquake was at quite a high level. When the Ms 8.0 earthquake occurred, many landslides were induced, including several large-scale landslides. As a result, it caused serious casualties and damage to road traffic (Xu et al. 2009). For a large number of landslides induced by the earthquake events, there is no special literature to systematically study the influence of post-rain earthquake. However, according to the meteorological data, there should be the impact of rainfall.

Sassa et al. (2007) analyzed the characteristics of landslides caused by Niigata earthquake in Japan in 2004 (M6.8) and the earthquake at Leyte Island in Philippines in 2006 (M2.6). The results showed that such a large-scale landslide disaster was the result of the combined action of earthquake and rainfall. Excessively high pore water pressure induced by the coupling of earthquake and rainfall formed an area with lower resistance, which led to the evolution of the slip surface along this area. Noteworthy, their analysis also showed that the location of the groundwater level caused by rainfall plays an important role in the formation, occurrence, and development of landslides. Faris and Wang (2014)

analyzed the initiation mechanism of Tandikat landslide induced by the Ms7.6 earthquake in West Sumatra, Indonesia on September 30, 2009. It was considered that the extensive and heavy rainfall before the earthquake caused the saturation of soil and accumulation of high pore-water pressure under the action of earthquake, which triggered the landslide. Consequently, it is important to study the effects of the unfortunate combination of otherwise independent events such as heavy rainfalls and earthquakes. Gong and Li (2012) used numerical simulation method to study the failure characteristics of loess landslides under the action of post-rain earthquake in Gansu Province. Wang and Pu studied the dynamic response and deformation evolution process of loess slope under earthquake after rainfall based on model tests in recent years (Wang et al. 2021; Pu et al. 2021). The results showed that seismic subsidence occurred in the middle of the crest of loess slope under the action of earthquake after rainfall, and the failure process of loess slope could be divided into four stages, namely, elastic deformation, rapid increase of residual deformation, liquefaction slip, and creep. The accumulated pore water pressure in the slope during the earthquake was observed. Martino et al. (2020) analyzed the failure characteristics of landslides induced by the $M_w 5.1$ earthquake in Italy on August 16, 2018, and pointed out that the unfortunate coupling of rainfall and earthquake was the main factor inducing landslides in this area. Rainfall led to the increase in soil saturation, which then resulted in landslides under the action of seismic force.

Recently, some studies have been carried out on homogeneous loess slopes (Pu et al. 2020). However, non-loess slopes are still in the initial stage of exploration, and a series of failure characteristics and failure mechanism of the slope need to be further investigated. The existing results cannot yet meet the requirements of slope disaster prevention and reduction. Excessive rain can render the sloping areas very vulnerable to landslides.

Many areas along Sichuan–Tibet railway get plenty of rainfall, and thus there is possibility of landslides induced by earthquake after events of heavy rainfall in this area. Therefore, in this study, the common deposit slopes along Sichuan–Tibet railway line would be considered as the prototype and a shaking table test would be conducted to study the failure characteristics of slopes with different soil

properties under the action of earthquake after events of heavy rainfall. The failure mode of the slope would be further investigated. Instant responses of moisture content and pore water pressure would be examined. The motion of soil particles would be investigated during slope failure, and the failure mechanism of slope would be also examined. Furthermore, the influence of soil properties on critical acceleration of slope failure would be analyzed.

2 Methods

2.1 Study area

The study area belongs to the Nyingchi–Bomi section of the Sichuan–Tibet line, which is located on the north side of the "big bend" of the Yarlung Zangbo River, the Landa Mountains-the confluence of the Himalayas, Nianqing Tanggula Mountains and Hengduan Mountains, and the northern margin of the eastern Himalayan tectonics (Figs. 1a and 1b). Owing to the special geological and geographical environment and climatic conditions, weathering of rocks in the

study area is relatively strong. Some slope surfaces are often subjected to weathering and lead to stripping of rock fragments, which get mixed with gravel, sand, clay, and other grained soil, forming a typical soil–rock stratigraphic structure type of landslide (Figs. 1c-1e). The slope angle of the area is 25°–80°, and the thickness of the slope is 3–60 m. The concentrated rainfall in the rainy season is heavy, earthquakes occur frequently, and the probability of landslides under the combined action of otherwise independent events of rainfall and earthquakes is very high.

2.2 Test apparatus

The test was performed on an electromagnetic shaking table with a size of 1.2 m × 1.2 m. The maximum acceleration that could be output by it was 5 g and the maximum displacement was 51 mm. A rigid model box with dimension of 2.0 m × 0.3 m × 1.7 m (length × width × height) was used, and the side wall of the box was made of transparent plexiglass board (Fig. 2). In order to reduce the boundary effect, a smooth film was pasted on the wall of the plexiglass plate. A coordinate reference ruler was set outside the
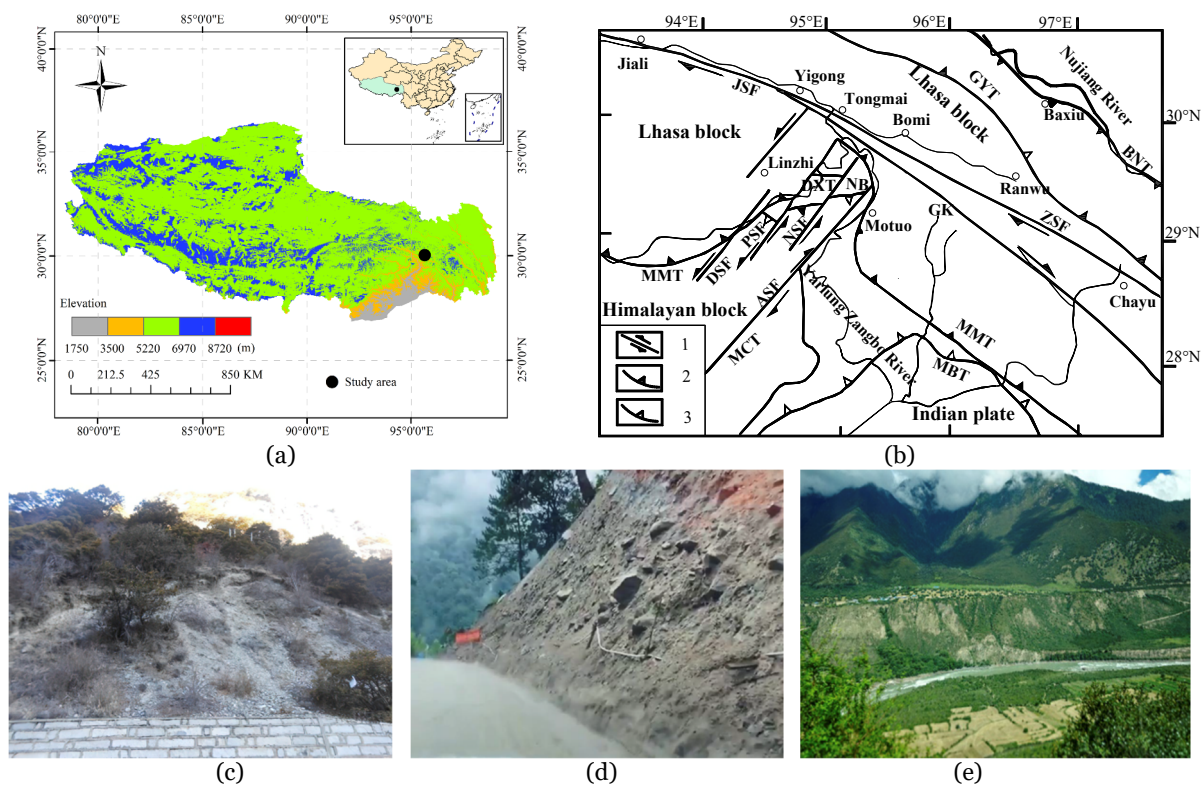
Fig. 1 (a) Location of the study area; (b) Geological structure of the study area in the eastern Tibetan region of the Himalayas; (c-e) Slope along the study area (c) slope with sandy soil; (d) slope with gravel and clay; and (e) slope with clay.

wall to observe the longitudinal deformation of the slope. Moreover, an artificial rainfall system was designed to simulate the rainfall, as shown in Fig. 2. The rainfall nozzles were installed at the top of the model box, and the rainfall intensity could be adjusted with the valve.
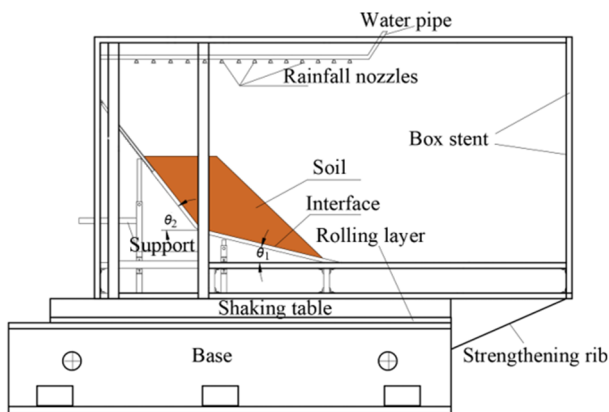

Fig. 2 Schematic illustration of the test apparatus.

2.3 Test model

Three types of slopes with different soil properties along the Nyingchi–Bomi section of the Sichuan–Tibet line (Fig. 1) were selected as the geological prototype. The prototype slopes are, respectively, slope with sandy soil (Model 1), slope with gravel and clay (Model 2), and slope with clay (Model 3). In this study, height of the prototype slope was set to be 15 m. The height of the model slope was 0.6 m, thus the geometric scale of similarity was 25. The slope angle was set to 44°. The angle of the bedrock interface with the horizontal was set to $\theta_1 = 14°$ and $\theta_2 = 52°$, respectively (Fig. 2). By using the Buckingham PI theorem (Buckingham 1914), the similarity relationship of physical quantities between the model and the prototype was obtained, as presented in Table 1. The mechanical parameters of soil in the prototype slope were determined by sampling the soil from the field and by conducting direct shear test. The strength parameters of prototype soil with different water content are shown in Fig. 3. The soil in model slope is composed of barite powder, quartz sand, and fly ash. The ratio of each component is determined according to the strength parameters of soil in model slope. The mean diameter of soil in model slope 1 is $d_{50}=0.3$ mm, $d_{50}=0.8$mm in model slope 2, and $d_{50}=0.05$ mm in model slope 3. The physical and mechanical properties of soil in model and prototype are

Table 1 Similarity relationship of physical quantities in model test

Physical parameters	Scaling law	Scale factor
Slope height (H)	C_H	25
Unit weight (γ)	C_γ	1
Gravity acceleration (g)	C_g	1
Cohesion (c)	$C_C = C_\gamma C_H$	25
Internal friction angle (φ)	1	1
Compression modulus (Es)	$C_{Es} = C_\gamma C_H$	25
Poisson's ratio (ν)	1	1
Rain intensity (q)	$C_q = C_H^{0.5} C_g^{0.5}$	5
Permeability coefficient (k)	$C_k = C_H^{0.5} C_g^{0.5}$	5
Main frequency of seismic load (f)	$C_f = C_H^{-0.5} C_g^{0.5}$	0.2
Time (t)	$C_t = C_H^{0.5} C_g^{-0.5}$	5

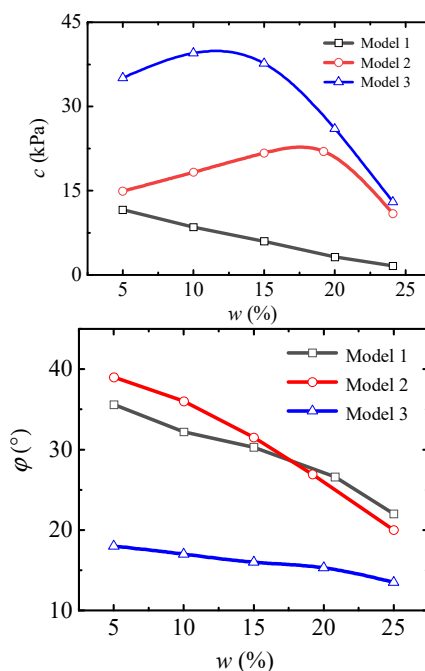**Fig. 3** Variation of cohesion (c) and internal friction angle (φ) with different water contents (w) (Model 1: slope with sandy soil, Model 2, slope with gravel and clay, Model 3, slope with clay).

summarized in Table 2. The model slope was constructed by layered filling method, and the soil in each layer of 10 cm was compacted by constant external force to ensure the uniform porosity of the slope. After the model slope was constructed, the compactness of soil that makes up the slope was tested. The tested results show that the soil within the three model slopes is slightly dense. Furthermore, banded white sand was set on both the side walls of the slope to observe the slope deformation. In the test, the rainfall was simulated to occur continuously for 210 min with the constant intensity of 2.38 mm h⁻¹,

**Table 2** Soil properties in model and prototype

Soil	Model/ prototype	Natural unit weight (kN/ m³)	Compression modulus E_s (MPa)	Cohesion C (kPa)	Internal friction angle (°)	Permeability coefficient (mm/s)	Water content (%)
Model 1	Model	15.6	12.7	0.7	28.8	0.031	8.8
	Prototype	15.2	39.6	9.1	32.9	0.155	8.9
Model 2	Model	16.7	11.8	2.7	30.3	0.062	9.5
	Prototype	16.1	46.9	17.5	36.8	0.310	8.7
Model 3	Model	15.9	11.2	4.5	18.1	0.006	12.3
	Prototype	16.4	29.4	38.8	33.8	0.031	11.8

which belongs to heavy rain.

2.4 Instrumentation

The pore water pressure sensor (precision: 10 Pa, measuring range: 0-10 kPa, accuracy: 0.1%) and water content sensor (EC-5, Decagon company, USA, accuracy: 1%) were used in the test. The acceleration sensor with a range of 0-2 g (Silicon Design Company, USA, accuracy: 1%) was used to monitor the acceleration of slope. In the course of the test, the particle image velocimeter was employed to record the particle velocity of soil. Moreover, an accelerometer was arranged on the shaking table to monitor the input acceleration. The detailed arrangement is shown in Fig. 4.
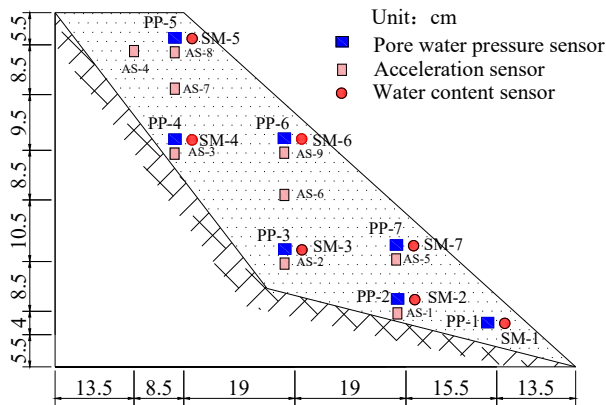
Fig. 4 Arrangement of measuring sensors in the test.

2.5 Input motions

The Wenchuan earthquake wave （travelling in an East-West direction from the measuring point at Marchoki Station in Ma-er-kang city）with different amplitudes was selected as the input seismic wave. The duration of the input wave was 20 s, and the amplitude of loading wave was increased at an interval of 0.1 g until it reached the critical value of slope instability. Typical time history and response spectrum of acceleration are shown in Fig. 5.

3   Results and Discussions

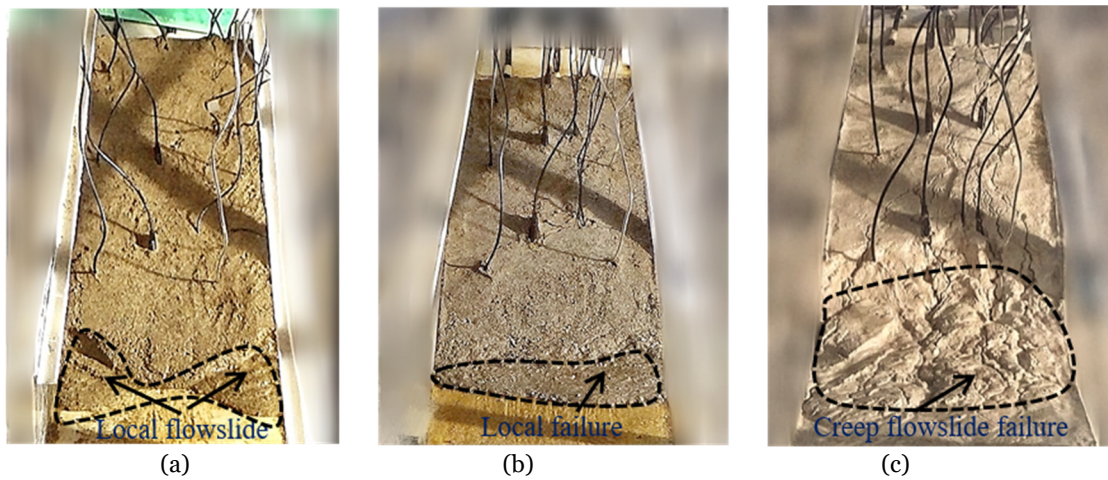### 3.1 Failure characteristics of soil slope under heavy rainfall

After rainfall infiltration, rainwater converges to the foot of the slope under the action of gravity. Thus, the water content of soil at the foot of the slope increases and the shear strength decreases. After the rainfall of 210 min, three types of slopes exhibited different failure characteristics, and the following three failure modes were observed: local flowslide, local failure, and creep flowslide failure. Fig. 6a shows that local flowslide occurs at the foot of slope with sandy soil (Model 1).In contrast, the local failure occurs at the foot of slope with gravel and clay (Model 2), and the overall deformation area is larger than that of Model 1, as shown in Fig. 6b. Owing to the fine grain size of clay (Model 3), creep flowslide failure mode emerges at the bottom, and also obvious runoff erosion failure occurs on the slope surface (Fig. 6c).

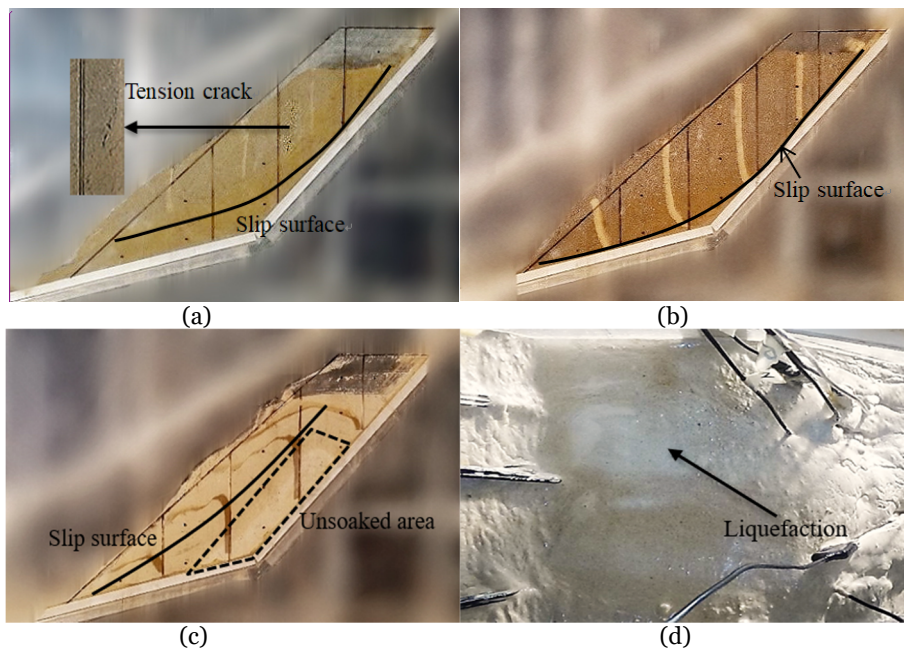### 3.2   Failure mode of the slope under earthquake after rainfall

At the end of the rainfall, a seismic load was applied to the slope until failure occurred. Fig. 7 shows the failure mode of the slope with different soil properties, exhibiting significant differences in the failure modes of the slope with different soil properties. The three failure modes, namely, local slip failure, overall slip failure, and shallow scouring and creep flowslide failure correspond to three slopes, respectively. The slope with sandy soil (Model 1) presents a local slip failure mode, which indicates that the upper part slides along the bedrock interface and the lower part develops within the overburden layer (Figs. 7a). The slope with gravel and clay (Model 2)
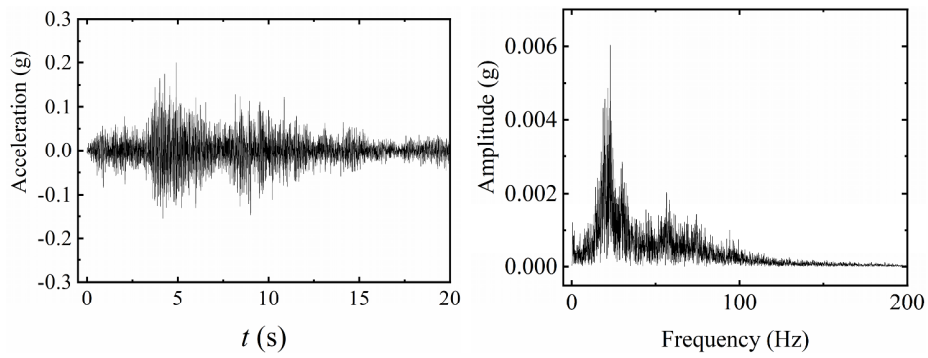
Fig. 5 Time history and Fourier spectrum of the Wolong seismic wave (0.2 g).

(a)   (b)   (c)

Fig. 6 Failure characteristics of slope under rainfall event: (a) Local flowslide mode in slope with sandy soil; (b) Local failure mode in slope with gravel and clay; and (c) Creep flowslide and runoff erosion mode in slope with clay.

(a)   (b)

(c)   (d)

Fig. 7 Failure mode of slope under earthquake after rainfall: (a) Local slip failure mode in slope with sandy soil ; (b) Overall slip failure mode in slope with gravel and clay; (c) Shallow scouring and creep flowslide failure mode in slope with clay; (d) Liquefaction at the top in slope with clay.

exhibits the overall slip failure mode, which indicates that the overlying layer slides entirely along the bedrock interface (Figs. 7b). The slope with sandy clay (Model 3) shows a shallow scouring and creep flowslide failure mode (Figs. 7c). The peak acceleration of slope instability for Model 1 is 0.790 g, and the final settlement at the top of the slope is about 9 cm. Moreover, tensile cracks with a length of about 11 cm appear in the middle and upper part of the slope in the process of slope failure under the action of reciprocating tension and shear. The failure peak acceleration of the Model 2 is 1.150 g, and the final settlement at the top of the slope is about 5 cm. The slip surface depth of sandy clay slope is the shallowest, and the peak acceleration at failure is 0.45 g. Furthermore, obvious liquefaction can be observed at the top of the slope (Fig. 7d).

3.3 Variation of volumetric moisture content

The variation of volumetric moisture content at different locations of the slope during rainfall is shown in Fig. 8. The figure illustrates that the moisture content of the soil in three types of slopes increases with the rainfall time, but each of them also has its own unique characteristics. Noteworthy, the permeability of slope with sandy soil (Model 1) and slope with gravel and clay (Model 2) is larger, and the responses of moisture content of each point in the two slopes are similar. On the other hand, the permeability of slope with sandy clay (Model 3) is obviously smaller, and the variation of moisture content of soil in this slope is obviously different from those of the other two. Moreover, the moisture content of soil (SM-1) at the toe of Model 1 and Model 2 increases first, while that of soil on surface (SM-6) in the middle and upper part of Model 3 increases at the earliest. With the increase of rainfall duration, the soil moisture contents at the middle and lower interface of Model 1 and Model 2 and the shallow part of Model 3 increase rapidly.

Furthermore, the volumetric water content responses of SM-1, SM-5, SM-6, and SM-7 on the surfaces of Model 1 and Model 2 slope occur earlier than those of SM-2, SM-3, and SM-4 inside the slope. When the volume water content is stable, rainwater converges at the bedrock interface and the volumetric water contents of SM-1, SM-2, and SM-3 near the bedrock interface in the middle and lower part of the slope become higher than those of other
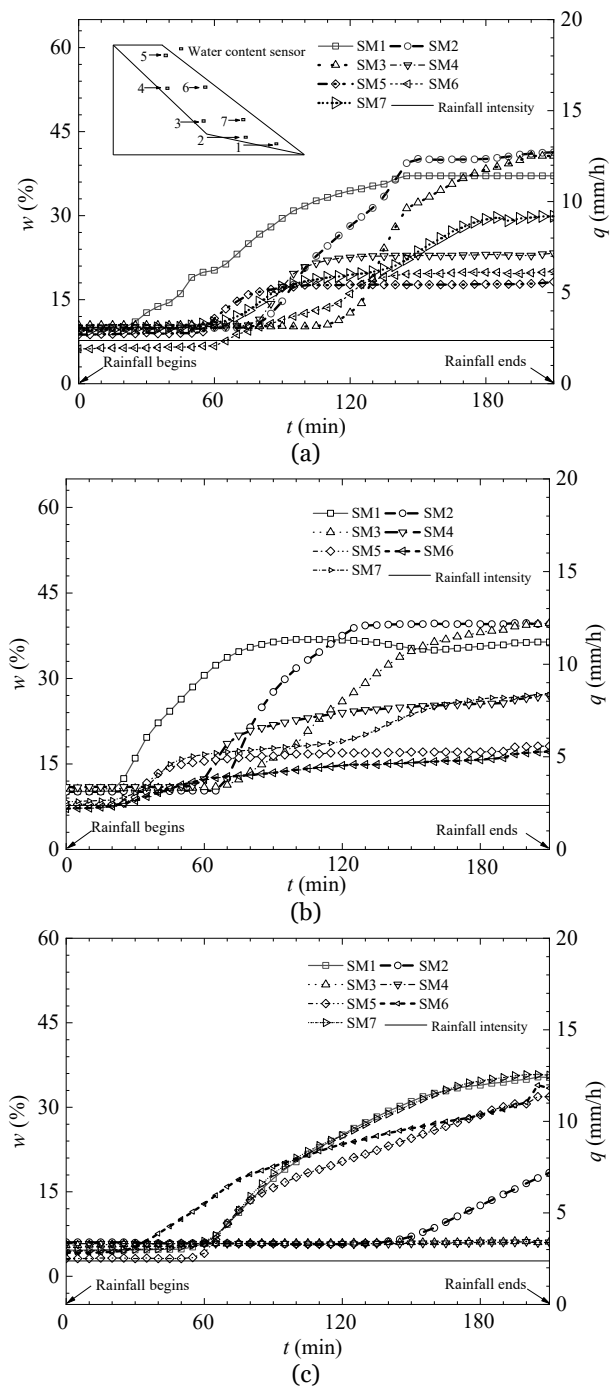
Fig. 8 Variation of volumetric water content in slope during 210 min of rainfall: (a) Model 1; (b) Model 2; and (c) Model 3.

points. Obviously, the response of the soil located in the deeper part of Model 3 occurs later than that in shallower layer, e.g., the moisture contents of SM-3 and SM-4 have no obvious change during rainfall. For Model 3, rainwater mainly flows in the shallow layer, which does not cause rainwater to converge at the bedrock interface, but rainwater exhibits a strong

surface erosion effect on the slope. The above-mentioned analysis indicates that the grain size of soil particle significantly influences the response of moisture content of soil in this slope. The soil with high moisture content is more likely to lose stability.

3.4 Variation of pore water pressure

Fig. 9 shows the variation of pore water pressure at different locations of Model 1 during rainfall, which is similar to that of water content. Fig. 10 presents the contour of pore water pressure in the slope of Model 1. With the progress of rainfall, the pore water pressure begins to increase from the foot of the slope
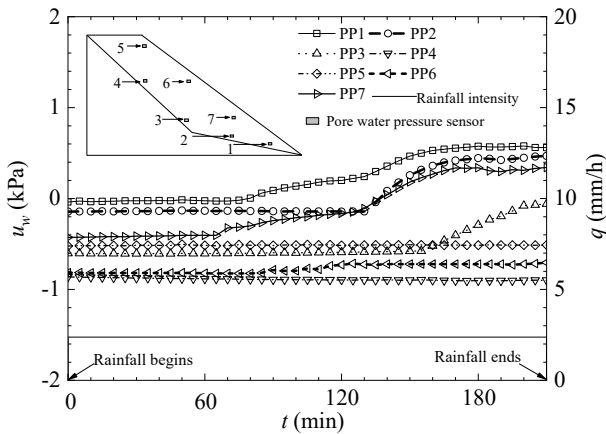

Fig. 9 Variation of pore water pressure (u_w) in slope with sandy soil during 210 min of rainfall.

and gradually develops at the top of the slope. The larger elevation corresponds to the smaller increase of pore water pressure. Noteworthy, the top of the slope is always in a state of negative pore pressure. During the earthquake, the pore water pressure in Model 1 varies with the peak value of the vibration waveform, as shown in Fig. 11. Furthermore, the response of pore water pressure indicates that even after many times of vibration at some points, the pore water pressure returns to the original level when the vibration stops, indicating that there is almost no cumulative effect of pore water pressure, and this case, the soil mainly produces elastic deformation. After repeated vibration in some positions of the slope, the pore water pressure gets obviously accumulated, indicating that the soil undergoes plastic deformation. Finally, the results reveal that the variation range of pore water pressure is the largest in places with higher water content, indicating that the increase of water content leads to the enhancement of the dynamic pore water pressure during earthquake and aggravate the risk of slope failure.

Figs. 12-14 show the responses of pore water pressure in Model 2. Different from Model 1 (slope with sandy soil), the pore water pressure in Model 2 (slope with gravel and clay) varies mainly at the bedrock interface. Notably, the pore water pressure begins to increase from PP-1 and PP-4 at the bedrock interface and develops toward the middle (Fig.
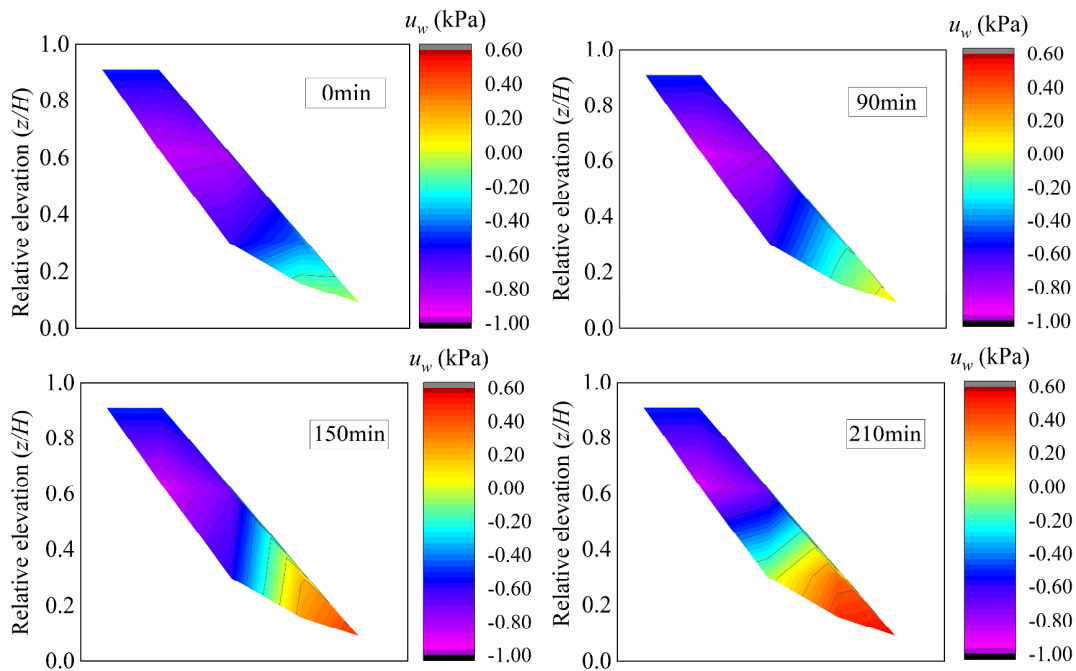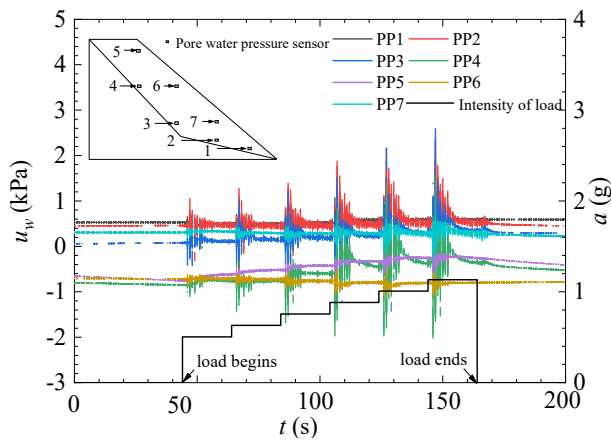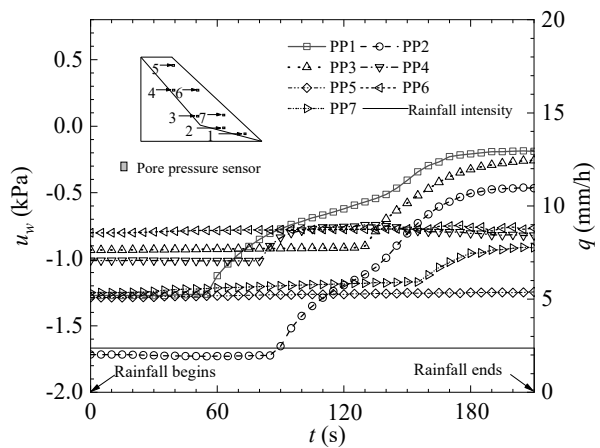

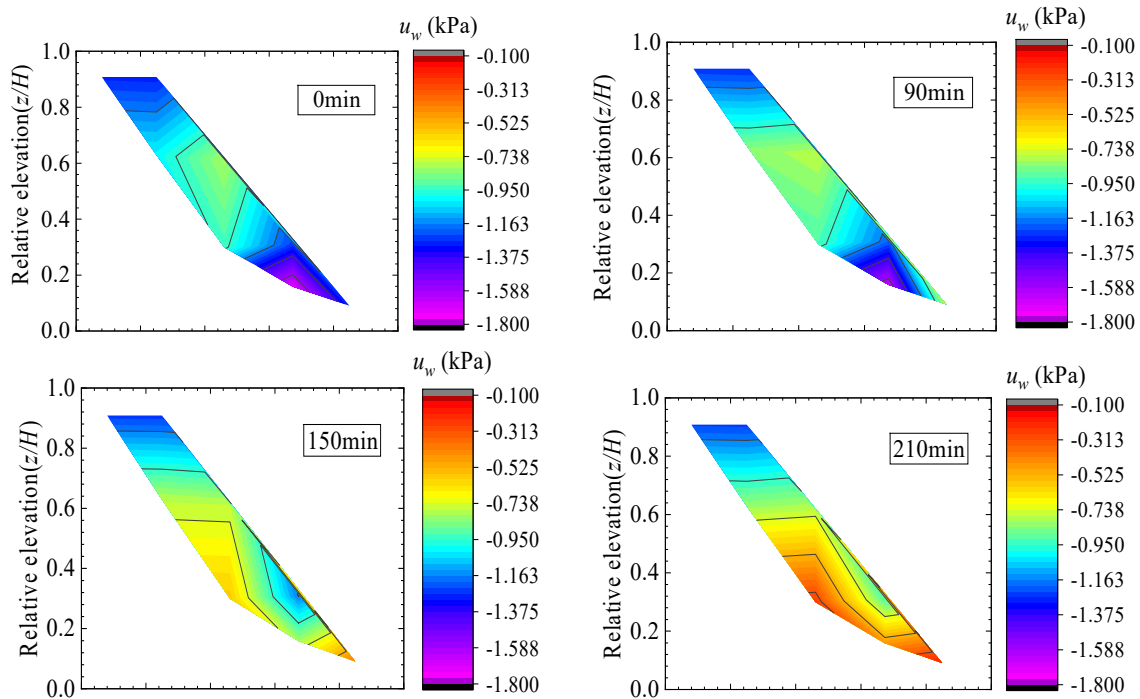**Fig. 10** Contour of pore water pressure in slope with sandy soil during 210 min of rainfall.

Fig. 11 Variation of pore water pressure in slope with sandy soil during seismic loading when 210 min rainfall ends.

Fig. 12 Variation of pore water pressure in Model 2 (slope with gravel and clay) during 210 min of rainfall.
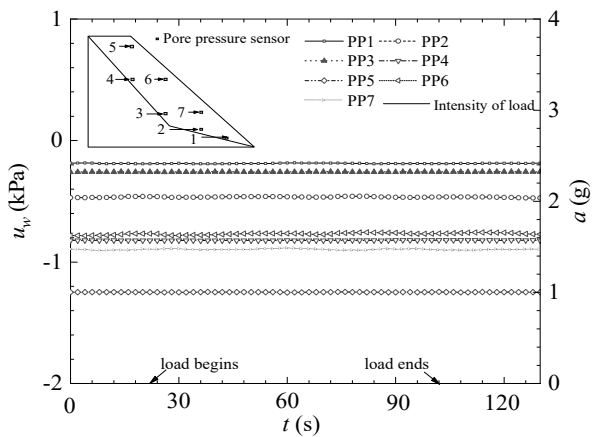

Fig. 13 Contour of pore water pressure in Model 2 (slope with gravel and clay) during 210 min of rainfall.

12). Moreover, compared with Model 1, the pore water pressure in the middle and upper part of Model 2 also increases (Fig. 13). Finally, the pore water pressure in the slope at the bedrock interface is higher than that at the slope surface, and the pore water pressure at the foot of Model 1 is also higher.

Compared with Model 1, Model 2 has almost no obvious dynamic pore water pressure during vibration (Fig. 14). It clearly indicates that the pore water pressure induced by vibration in Model 2 can dissipate rapidly, as a result, Model 2 exhibits a stronger ability to bear dynamic pore water pressure. In this case, the slope failure is mainly caused by the direct action of ground motion. Therefore, slope failure often requires greater seismic peak acceleration in this condition.

Figs. 15-17 present the responses of pore water pressure in Model 3. Different from Model 1 and Model 2, the pore water pressure at shallow layer of overlying soil mass in Model 3 varies significantly during rainfall (Fig. 15), but not at the remaining part of the model. The contour of pore water pressure also illustrates its significant difference from Model 1 and Model 2 (Fig. 16). The pore water pressure in Model 3 decreases from the surface to the interior, and the peak value appears on the surface.

Fig. 14 Variation of pore water pressure in Model 2 (slope with gravel and clay) during seismic loading when 210 min of rainfall ends.
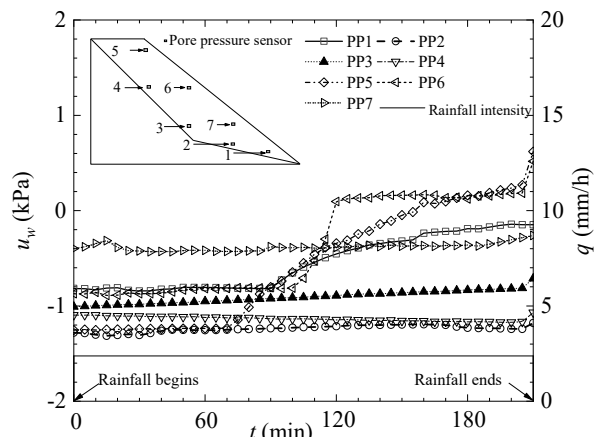
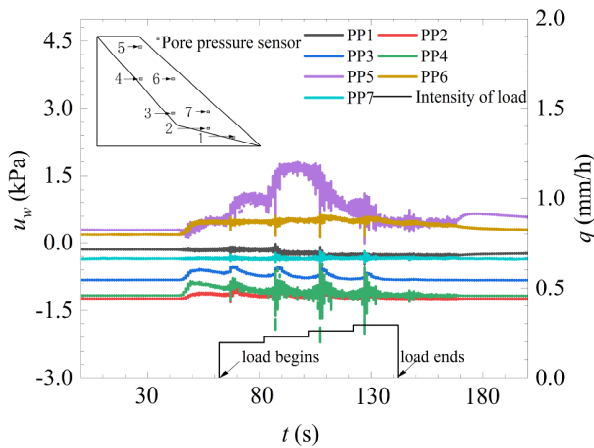**Fig. 15** Variation of pore water pressure in Model 3 during 210 min of rainfall.
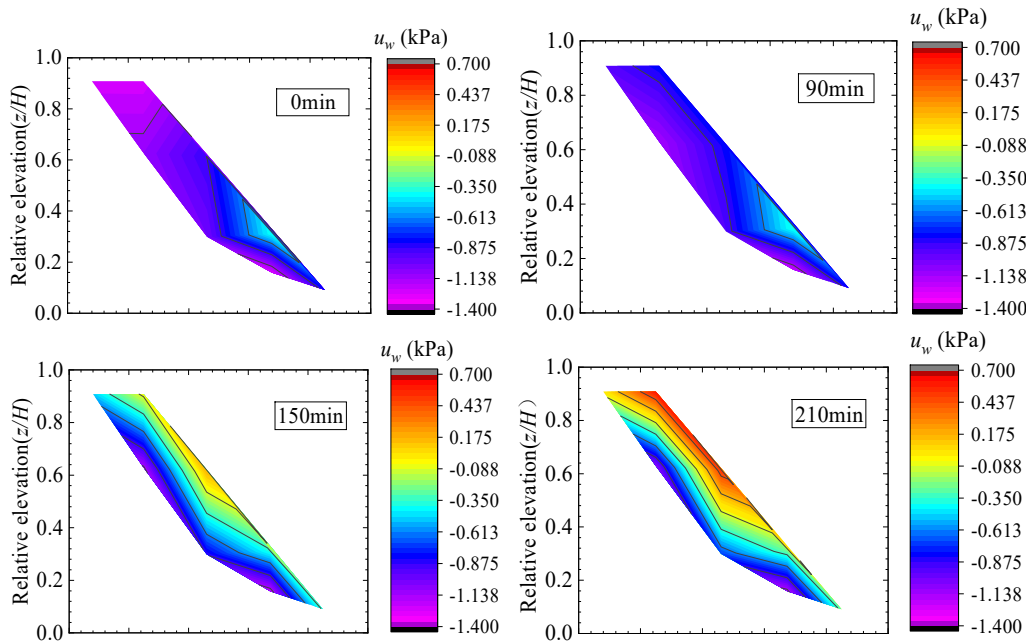
Fig. 16 Contour of pore water pressure in Model 3 during 210 min of rainfall.

Fig. 17 shows the variation of pore water pressure during earthquake. In the process of earthquake, the slope exhibits cracks in many places, resulting in serious deformation and damage. Therefore, pore water pressure leads to irregular changes in the parts with higher water content (e.g., at PP-5 and PP-6). Noteworthy, the pore water pressure at PP-6 does not increase obviously in the process of vibration. During earthquake, a large deformation occurs near the PP-5 point, and a distinct cumulative effect of pore water pressure is observed.

The above-mentioned analysis indicates that Model 3 is sensitive to dynamic pore water pressure induced by ground motion. The coupling effect

between dynamic pore water pressure and earthquake leads to the significant decrease in the stability of the slope.

Based on the above-mentioned analysis, the response of pore water pressure in slope exhibits the following characteristics: during rainfall, the response of pore water pressure shows hysteresis effect. The water content of soil first increases, and then pore water pressure increases. Noteworthy, with different soil properties, the spatial distribution of pore water pressure is different in the slope. The peak pore water pressure in the slope with high permeability of soil occurs mainly near the foot of the slope and near the bedrock interface in the middle and lower parts of the

Fig. 17 Variation of pore water pressure in Model 3 during seismic loading when 210 min of rainfall ends.

slope. However, for the slope with low permeability of soil, the peak value of pore water pressure decreases from the surface to the interior. Consequently, under the action of earthquake, the responses of the pore water pressure in slopes with different soil properties are quite different. The soil properties of slope affect not only the infiltration mode of rainfall, but also the variation mode of excess pore water pressure under the effect of earthquake.

### 3.5 Motion of soil particles in slope during slope failure

Fig. 18 presents the speed contour of soil particles during slope failure. The speed contour of the soil particles in Model 1 under the action of earquake wave with a peak value of acceleration of 0.3g is shown in Fig. 18a. A clear velocity zone is observed in the slope, i.e. high-speed and low-speed area. The velocity above the slip surface is larger (about 67 mm s⁻¹), while that below it is smaller (about 30 mm s⁻¹). Owing to the large velocity difference, the slope is prone to shear dislocation near the velocity interface. Fig. 18b demonstrates that there is no obvious velocity zoning in the interior of slope exerted by a peak value of 0.4g wave, and the magnitude and direction of the velocity are nearly consistent, thus the overall failure mode occurs along the soil–rock interface. The speed contour of soil particles in Model 3 under the action of 0.1g peak acceleration is shown in Fig. 18c. The soil particle's speed of the shallow layer in Model 3 is larger (about 10 mm s⁻¹), and that at the other part in the slope is relatively small, thus the shallow layer slip occurs in the slope. The higher velocity area in Model 3 is
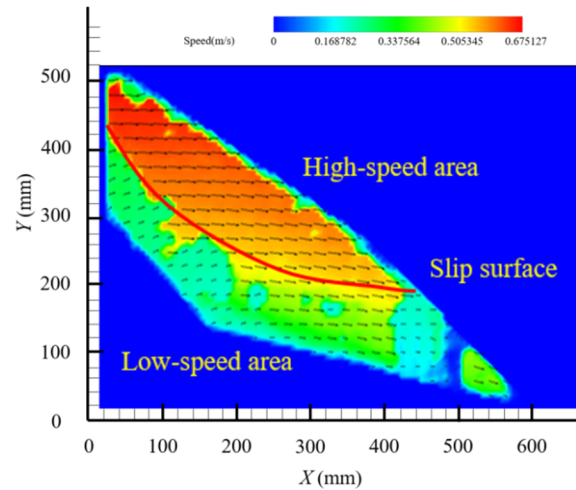
(a) Model 1 (at a peak value of acceleration of 0.3g)
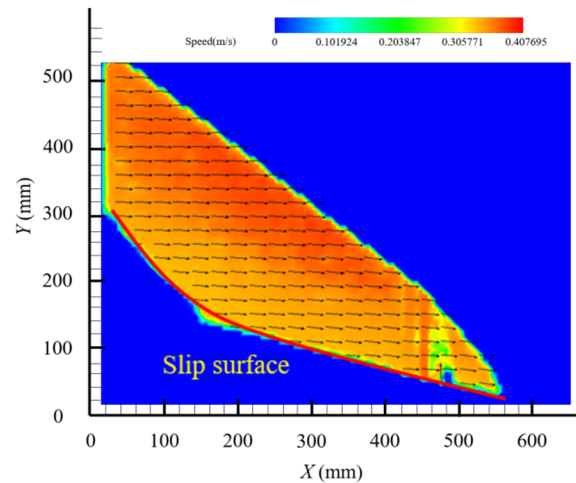
(b) Model 2 (at a peak value of acceleration of 0.4g)
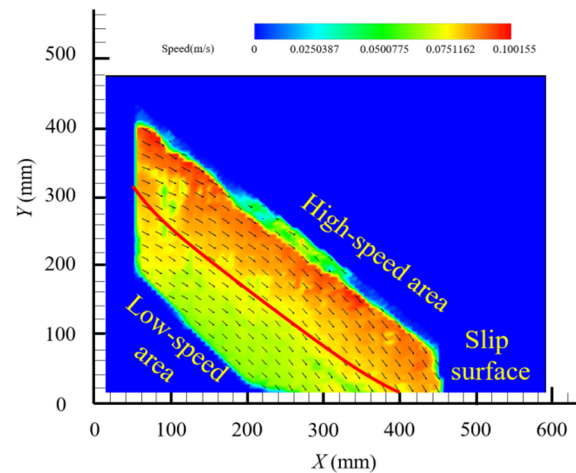
(c) Model 3 (at a peak value of acceleration of 0.1g)

Fig. 18 Contour of soil particle's speed at the time of failure.

concentrated in the part with higher water content and pore water pressure, indicating that the

distribution of water content and pore water pressure significantly impacts the failure mode of Model 3 under earthquake.

3.6 Critical Acceleration for Slope Failure

Different types of soil lead to significant differences in the peak acceleration for slope failure. In the test the amplitude of loading wave was increased at an interval of 0.1 g. When the slope has obvious deformation, and at this time the acceleration acting on the slope was defined as critical acceleration. Fig. 19 shows the critical acceleration for slope failure with different soil properties under the action of earthquake. The results show that the critical acceleration of slope with coarse-grained soil is greater than that of slope with fine-grained soil. Under the coupling action of earthquake and dynamic pore water pressure, the slip surface in Model 3 becomes shallower and the critical acceleration is the smallest. In contrast, the overlying soil in Model 2 slides along the bedrock interface under the action of earthquake, and the critical acceleration is the largest. The sliding surface depth in Model 1 is between those of Model 2 and Model 3, thus the critical acceleration required for slope failure is between the two.
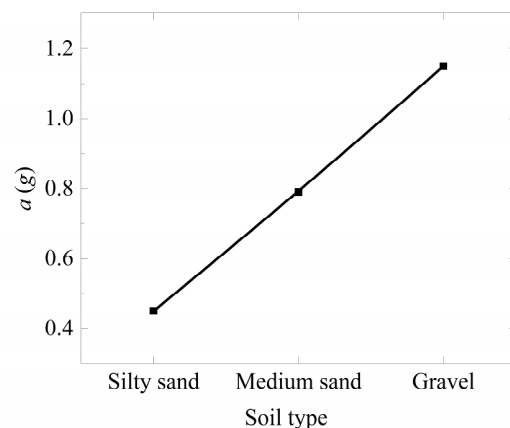
4   Conclusions

The failure characteristics and mechanism of deposit slope with different soil properties under earthquake after heavy rainfall event were studied by a shaking table test, and some conclusions can be drawn as follows:

(1) Significant differences are observed in the failure modes of the slope with different soil properties under earthquake after rainfall. There exist three failure modes, i.e., local slip failure, overall slip failure, and shallow scouring and creep flowslide failure.

(2) With different soil properties, the spatial distribution of pore water pressure is different in the

Fig. 19 Critical acceleration of slope instability in different soil types.

slope. The peak pore water pressure in the slope with high permeability of soil occurs mainly near the foot of the slope and near the bedrock interface in the middle and lower parts of the slope. However, for the slope with low permeability of soil, the peak value of pore water pressure decreases from the surface to the interior.

(3) Under the action of earthquake, the responses of the pore water pressure in slopes with different soil properties are quite different. The soil properties of slope affect not only the infiltration mode of rainfall, but also the variation mode of excess pore water pressure under earthquake.

(4) The grain size of soil particle significantly influences the response of moisture content of soil in this slope. There is an obvious velocity zoning during the failure of the slopes. Different types of soil lead to significant differences in the peak acceleration of slope failure. The critical acceleration of slope with coarse-grained soil is greater than that of slope with fine-grained soil under the action of earthquake.

Acknowledgements

References

Buckingham E (1914) On physically similar systems: illustrations of the use of dimensional equations. Phys Rev 4(4): 345-376.
https://doi.org/ 10.1103/PhysRev.4.345
Faris F, Wang FW (2014) Investigation of the initiation mechanism of an earthquake- induced landslide during

rainfall: a case study of the Tandikat landslide, West Sumatra, Indonesia. Geoenviron Disasters 1(1):1–18.
https://doi.org/10.1186/s40677-014-0004-3

Gong WJ, Li MY, Wu ZZ (2012) Stability Analysis of Landslide under Coupling Action of Earthquake and Rainfall—Taking the No. Ⅲ Landslide of Xihe County, Gansu Province as An Example. Northwestern Seismol J 34(2): 161-166. (In Chinese)
https://doi.org/10.3969/j.issn.1000-0844.2012.02.0161

Lin ML, Wang KL (2006) Seismic slope behavior in a large-scale shaking table model test. Eng Geol 86(2-3): 118-133.
https://doi.org/10.1016/j.enggeo.2006.02.011

Martino S, Antonielli B, Bozzano F, et al. (2020) Landslides triggered after the 16 August 2018 Mw 5.1 Molise earthquake (Italy) by a combination of intense rainfalls and seismic shaking. Landslides 17(5): 1177–1190.
https://doi.org/10.1007/s10346-020-01359-w

Pu XW, Wang LM, Wang P, et al. (2020) Study of shaking table test of seismic subsidence loess landslides induced by the coupling effect of earthquakes and rainfall. Nat Hazards 103(1):923–945.
https://doi.org/10.1007/s11069-020-04019-3

Pu XW, Wang LM, Wang P (2021) Initiation mechanism of mudflow-like loess landslide induced by the combined effect of earthquakes and rainfall. Nat Hazards 105(3):3079–3097.
https://doi.org/10.1007/s11069-020-04442-6

Qiu HZ, Kong JM, Wang RC, et al. (2017). Response mechanism of post-earthquake slopes under heavy rainfall. J Seismol 21(4): 869-884.
https://doi.org/10.1007/s10950-017-9641-9

Sassa K, Fukuoka H, Wang FW, et al. (2007) Landslides induced by a combined effect of earthquake and rainfall. Prog Landslide Sci 193–207.
https://doi.org/10.1007/978-3-540-70965-7_14

Shi J, Wang WX, Wen JX (2010) Meteorological anomalies before and after Wenchuan earthquake. Astro Res Technol 7(1):78-84+87+85. (In Chinese)
https://doi.org/10.14005/j.cnki.issn1672-7673.2010.01.011

Song SW (2009) Analysis and Investigation on Seismic Damages of Projects Subjected to Wenchuan Earthquake. Beijing: Science Press. (In Chinese)

Tian YY, Xu C, Xu XW, et al. (2016) Detailed inventory mapping and spatial analyses to landslides induced by the 2013 Ms 6.6 Minxian earthquake of China. J Earth Sci-china 27(6): 1016–1026.
https://doi.org/10.1007/s12583-016-0905-z

Tiwari B, Ajmera B, Tran D (2017) Influence of post-earthquake rainfall on the stability of clay slopes (IPL-192). In Workshop on World Landslide Forum. Springer, Cham. pp. 429-436.

Wang Q, Wang ZM, Su YQ, et al. (2021) Characteristics and mechanism of the landslide in Yongguang village, Minxian County, China. Nat Hazards 105(2):1413–1438.
https://doi.org/10.1007/s11069-020-04360-7

Xu C, Shen LL, Wang GL (2016) Soft computing in assessment of earthquake-triggered landslide susceptibility. Environ Earth Sci 75(9).
https://doi.org/10.1007/s12665-016-5576-7

Xu Q, Pei XJ, Huang RQ, et al. (2009) Large-Scale Landslides Induced by Wenchuan Earthquake, Science Press, Beijing. (In Chinese)

Yang B, Luo Y, Jeng DS, et al. (2019) Effects of moisture content on the dynamic response and failure mode of unsaturated soil slope subjected to seismic load. B Seismol Soc Am 109(2): 489-504.
https://doi.org/10.1785/0120180222

Yang B, Zhou ZH, Hou JR, et al. (2022) Failure characteristics and mechanism of deposit slopes with bedrock for different soil moisture contents under seismic load. Soil Dyn Earthq Eng 154:107128.
https://doi.org/10.1016/j.soildyn.2021.107128

Zhuang Y, Xing AG, Cheng QG, et al. (2020) Characteristics and numerical modeling of a catastrophic loess flow slide triggered by the 2013 Minxian–Zhangxian earthquake in Yongguang village, Minxian, Gansu, China. B Eng Geol Environ. 79(1): 439–449.
https://doi.org/10.1007/s10064-019-01542-x